Corrosion Science 247 (2025) 112776

Contents lists available at ScienceDirect

Corrosion Science

journal homepage: www.elsevier.com/locate/corsci

Exploring mechanisms and efficacy of passivation films in blocking hydrogen

Zhiyu Du [a], Rongjian Shi [a,b,*], Zhishan Mi [c], Zhao Xu [a], Yujie Zhu [a], Saiyu Liu [a], Kewei Gao [a], Alex A. Volinsky [d], Xiaolu Pang [a,b,*]

[a] Beijing Advanced Innovation Center for Materials Genome Engineering, School of Materials Science and Engineering, University of Science and Technology Beijing, Beijing 100083, China
[b] State Key Laboratory of Nuclear Power Safety Technology and Equipment, University of Science and Technology Beijing, Beijing 100083, China
[c] Research Institute of Advanced Materials (Shenzhen) Co., Ltd., Shenzhen 518045, China
[d] Department of Mechanical Engineering, University of South Florida, 4202 E. Fowler Ave. ENG030, Tampa 33620, USA

ARTICLE INFO

Keywords:
Passivation films
Hydrogen embrittlement
Hydrogen blocking
Austenitic stainless steel
Surface design

ABSTRACT

Based on hydrogen embrittlement-resistant surface design principles, this study investigates the microstructure and effectiveness of passivation films in blocking hydrogen. Passivation films, prepared by electrochemical methods, consist of outer FeOOH layer and inner layers of Cr_2O_3 and Fe_2O_3. The FeOOH layer, with a hydrogen adsorption capacity of −3.555 eV and a diffusion barrier of 3.766 eV, effectively prevents hydrogen penetration. The Cr_2O_3 and Fe_2O_3 layers enhance bonding between the films and the substrate as transitional layers. This synergistic structure enhances hydrogen-blocking capabilities, resulting in a 59.92 % reduction in hydrogen embrittlement sensitivity index and a 41.27 % decrease in brittle zone depth.

1. Introduction

Hydrogen embrittlement (HE)-resistant surface design aims to enhance the material surface or form a hydrogen barrier layer on or just beneath the surface. The principles of hydrogen blocking are as follows [1]. 1) Enhancing the diffusion barrier from the surface to the interior to impede hydrogen penetration. 2) Reducing hydrogen adsorption energy to suppress the dissociation of hydrogen molecules (or water molecules). 3) Facilitating the recombination of hydrogen atoms into hydrogen molecules and their subsequent release to minimize hydrogen accumulation within the material. The penetration and accumulation of hydrogen atoms can degrade the internal mechanical characteristics of the material, leading to the start and spread of fractures, thereby posing a serious threat to the structural integrity of the material [2,3]. Therefore, finding a simple and effective method for HE-resistant surface design is crucial to ensure material performance in harsh environments.

Current surface design for HE-resistant primarily involve introduction of alloying elements or application of surface coatings. Adding Si to twinning-induced plasticity steel forms a bilayer of (Fe, Mn)O and (Fe, Mn)$_2$SiO$_4$ on the surface [4], effectively inhibiting hydrogen permeation into the interior. (TiVAlCrZr)O coatings on 316L stainless steel obtained by magnetron sputtering and oxidation treatment significantly reduce hydrogen permeation rates [5]. Graphene oxide-alumina composite [6] and MXene [7] coatings prepared by sol-gel and spin-coating methods, respectively, have also demonstrated excellent hydrogen blocking performance. Although these methods effectively enhance resistance to HE, they typically involve complex fabrication processes, have inadequate adhesion between the coating and the substrate, and high production costs [8–10]. Compared with traditional methods of designing HE-resistant surfaces, passivation films offer a cost-effective approach utilizing natural or electrochemical formation methods. Passivation films developed on the surface of stainless steel at room temperature are typically only a few nanometers thick [11,12]. Denser and thicker oxide passivation layers can be formed by anodic polarization on stainless steel surfaces, significantly enhancing corrosion resistance [13–15]. The formation of passivation films are affected by various factors, including potential, temperature, and polarization duration, resulting in the passivation films thickness and composition variations [14,16–21]. Passivation films primarily consist of metal oxides, hydroxides, and bound water [22,23]. Extensive research has been carried out on the

* Corresponding authors at: Beijing Advanced Innovation Center for Materials Genome Engineering, School of Materials Science and Engineering, University of Science and Technology Beijing, Beijing 100083, China.
E-mail addresses: rongjianshi@ustb.edu.cn (R. Shi), pangxl@mater.ustb.edu.cn (X. Pang).

https://doi.org/10.1016/j.corsci.2025.112776
Received 6 November 2024; Received in revised form 26 January 2025; Accepted 10 February 2025
Available online 11 February 2025

corrosion resistance properties of passivation films. Ultra-thin 316L foils exhibited superior corrosion resistance in NaCl solution compared to deformed 316L, attributed to uniform, continuous, and dense Cr and Mo-rich passivation layer formed on the surface [14]. Similarly, double-layer passivation films formed on high entropy alloys (HEAs) with Co and Mo enriching the outer layer and Cr concentrating in the inner layer [24]. Despite a decrease in corrosion resistance of HEAs with temperature, the passivation-protected HEAs still exhibited better corrosion resistance than the untreated substrates. However, acidic electrolytes can lead to hydrogen release in corrosive environments, causing hydrogen atoms to accumulate on the metal surface and diffuse internally [25], leading to hydrogen-induced cracking [26].

Although passivation films have been extensively studied for their excellent corrosion resistance, their interaction with hydrogen and their impact on HE behavior remain areas that require further investigation. Previous studies have shown that hydrogen accumulation on the surface of stainless steel and within the intrinsic passivation films can weaken the protective effect of the film [27], and may even lead to the dissolution, degradation, or complete disappearance of the intrinsic passivation layer [28,29]. Hydrogen exposure causes the destabilization of passivation films, which is closely associated with the formation of defects within the film. These defects can impair the protective performance of the film [30,31]. Although previous studies have explored the potential effects of passivation films preparation methods on hydrogen blocking and emphasized the importance of further investigating the hydrogen-blocking mechanisms [32,33], research on the role of passivation films in improving HE behavior and their hydrogen-blocking mechanisms remains limited. Therefore, this study aims to further explore this area and address some of the gaps in existing research. In austenitic stainless steel, the susceptibility to HE is relatively low under normal conditions. However, prolonged exposure to hydrogen-rich environments or extreme conditions can lead to hydrogen ingress and material degradation. Compared to ferritic stainless steels, the passivation films formed on austenitic stainless steel substrates exhibit faster growth rates, higher coverage, and greater thickness [34]. Additionally, the Cr content of the passivation films on austenitic substrates is more uniform, resulting in less influence of grain orientation on their performance [35]. These characteristics provide significant advantages for austenitic substrates in hydrogen-blocking research. As a representative austenitic stainless steel, 316L is widely used in critical industrial applications such as hydrogen pipelines, storage tanks, and pressure vessels due to its excellent corrosion resistance and mechanical properties [36–38], making it an ideal material for investigating the hydrogen-blocking mechanisms of passivation films. While this study focuses on typical electrochemical conditions, it also opens opportunities to investigate more complex scenarios, such as the development of thicker films or modified compositions, in subsequent research [19,39].

Originating from the concept of HE-resistant surface design, this study confirms that passivation films significantly impede hydrogen, playing a crucial role in enhancing the material resistance to HE. Microstructure of passivation films and their ability to impede hydrogen permeation were investigated using various surface analysis and microstructure characterization techniques, along with theoretical calculations.

2. Experiments

2.1. Materials and microstructure characterization

An inductively coupled plasma-optical emission spectrometer (ICP-OES, Agilent 5900) and a carbon sulfur analyzer (CS230), as specified in Table 1, were used to ascertain the chemical composition of 316L stainless steel. To prepare the sample for microstructural analysis, the 316L stainless steel surface was sequentially polished using silicon carbide (SiC) sandpapers with grit sizes of 400, 1200, 2000, and 5000, followed by refinement with 2 μm and 1 μm diamond paste to achieve a smooth, mirror-like finish. The polished sample was then ultrasonically cleaned in acetone, alcohol, and deionized water to remove any residual polishing debris. Finally, the material was etched using a solution with a 90:7:3 vol ratio of HCl, HNO_3, and HF to reveal the microstructure. The morphology and phases of the material were examined using optical microscopy (OM, LEICA DM 2500 M) and an electron back-scatter diffraction (EBSD, Oxford Nordly Max3 detector). For EBSD analysis, samples were electro-polished using a mixture of 8 vol% perchloric acid and 92 vol% ethanol solution at −30 °C and 25 V potential for approximately 15 s. Channel 5 software was utilized to examine the grain morphology at a scanning step of 0.5 μm. Fig. 1 displays the microstructure of 316L stainless steel characterized by OM and EBSD with grain size distribution analysis. There is typical austenitic structure features of the steel with an average grain size of 13.2 ± 0.2 μm.

2.2. Electrochemical measurements

Samples were subjected to dynamic potential scanning in a 0.5 mol/L sulfuric acid (H_2SO_4) solution using a workstation connected to a traditional three-electrode cell with a saturated mercury/mercurous sulfate (Hg/Hg_2SO_4) electrode as the reference and platinum foil as the counter electrode. The working electrode was connected to the copper wire embedded in epoxy resin. The sample was sealed in resin, leaving a $10 \times 10\ mm^2$ surface exposed, and prepared using the same polishing procedure described earlier for microstructural analysis. The edges of the sample were smoothed to ensure a tight seal with the resin, eliminating any gaps, and the specimen was inspected under an OM to confirm the absence of defects such as bubbles or crevices before testing. In order to guarantee surface stability, the open circuit potential (OCP) was stabilized for 30 min before to the tests. Then, the potentiodynamic polarization was varied from −0.5 V to 1.2 V with 1 mV/s scanning frequency. After determining the voltage of the passivation region according to the polarization curve, the same electrolyte and three-electrode system were polarized for 4 h under constant potential. Cathodic pre-treatment was deliberately omitted to prevent any alteration of the initial native oxide films that could result from reduction before passivation. For each condition, three specimens were tested.

2.3. Characterization of passivation films

X-ray photoelectron spectroscopy (XPS, Thermo Scientific K-Alpha) was used to analyze the chemical composition of passivation films. To facilitate the calibration of the binding energy for internal reference, the C 1s peak was used with a binding energy of 284.8 eV, and background subtraction was applied. Subsequently, XPS PEAK 4.1 software was utilized to deconvolute and match the XPS spectra of the identified components. This procedure provided chemical composition of the passivation films, as well as the changes before and after passivation.

Time of flight secondary mass spectrometry (ToF-SIMS, 5–100 ION-TOF) was utilized for depth profiling elemental analysis of the naturally passivated (NP), acid passivated (AP), naturally passivated and 72 h hydrogen charged (NP-72h), and acid passivated and 72 h charged (AP-72h) samples. The specific experimental conditions for these four samples are summarized in Table 2. This instrument combines static SIMS

Table 1
Chemical composition of the 316L stainless steel.

Elements	C	Mn	P	S	Cr	Ni	Mo	Co	B
Concentration, wt%	0.035	1.29	0.035	0.0046	16.54	10.63	2.01	0.25	0.0031

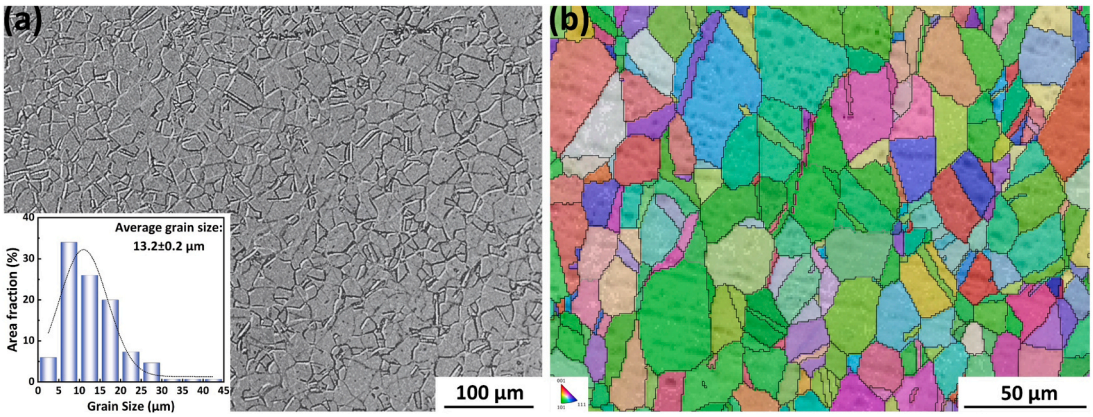

Fig. 1. Microstructure of the 316L stainless steel: (a) Optical image with a grain size distribution; (b) Inverse pole figure in the Z direction (IPF+BC+GB) map.

Table 2
Preparation conditions for four types of the 316L stainless steel samples.

Sample	Passivation process	Hydrogen charging conditions
NP	exposure to air at room temperature	/
AP	0.5 V in 0.5 mol/L H_2SO_4 for 4 h	/
NP-72 h	exposure to air at room temperature	−20 mA/cm^2 in 0.5 mol/L H_2SO_4 with 2 g/L thiourea (CH_4N_2S) for 72 h
AP−72 h	0.5 V in 0.5 mol/L H_2SO_4 for 4 h	−20 mA/cm^2 in 0.5 mol/L H_2SO_4 with 2 g/L CH_4N_2S for 72 h

and sputtering, employing a 45° incident angle Bi^{3+} primary ions (30 keV, 0.45 pA) for static SIMS over an area of 40 × 40 μm^2, and Cs^+ sputtering beam (0.5 kV, 78 nA) over an area of 120 × 120 μm^2. To mitigate edge effects, static SIMS was centered on the sputtering crater.

Utilizing energy-dispersive spectroscopy (EDS) in conjunction with a field emission transmission electron microscope (FETEM, Titan ETEMG2, USA), the thickness and elemental distribution of the passivation layer were examined. Cross-sectional TEM samples were prepared through focused ion beam (FIB) and ion-beam thinning methods.

2.4. Slow strain rate tensile and hydrogen content tests

Dog-bone-shaped tensile specimens with a gauge length of 12 mm and a cross-section of 3 × 1 mm^2 were prepared for testing. Hydrogen charging for the slow strain rate tensile (SSRT) tests and hydrogen content (HC) measurements was performed under the conditions summarized in Table 2. Immediately following hydrogen charging, the SSRT tests were performed using a universal testing machine (ETM504C, WANCE, China, 50 kN capacity) at a strain rate of 5 × 10^{-5} s^{-1}. Three specimens were tested for each condition. The fracture morphology of the SSRT specimens was subsequently analyzed using field emission scanning electron microscopy (SEM). The HE index (HEI) was calculated to evaluate the materials' susceptibility to HE [40]:

$$HEI = \frac{\delta_{H-uncharged} - \delta_{H-charged}}{\delta_{H-charged}} \times 100\% \quad (1)$$

Here, $\delta_{H\text{-}uncharged}$ and $\delta_{H\text{-}charged}$ represent the elongation to fracture of not charged and hydrogen-charged SSRT specimens, respectively.

Bruker hydrogen analyzer (G4 PHOENIX DH, Germany) was used to measure the HC of the hydrogen-charged specimens for 10 min at 800 °C.

2.5. Density functional theory calculations

The diffusion energy barriers of hydrogen in FeOOH, α-Cr_2O_3, α-Fe_2O_3, and fcc-Fe bulk structures were studied by using the first-principles calculation method based on the density functional theory (DFT) in the Vienna ab initio simulation package (VASP) [41]. The projector augmented wave (PAW) [42] method was applied to describe the core electrons and the electron exchange, and the correlations were modeled with the Perdew-Burke-Ernzerhof (PBE) method [43]. All structures were totally relaxed, the residual stress on each atom was less than 0.01 eV/Å, and the total energy converged to 10^{-6} eV/atom for calculations. For all structures, a 5 × 5 × 5 k-point mesh was used in the Monkhorst-Pack grids to sample the Brillouin zone (BZ). Based on the principles of transition state theory and the Arrhenius equation, the diffusion coefficient of a hydrogen atom can be determined using the following formula [44,45]:

$$D\ (T) = l^2 \nu \exp\left(-\frac{E_{diff}}{kT}\right) \quad (2)$$

where l represents the hop distance, ν is the attempt frequency, E_{diff} denotes the activation energy for hydrogen diffusion, k is the Boltzmann constant, and T is the temperature. The hop distance (l) and attempt frequency (ν) are derived from DFT simulation.

3. Results and discussion

3.1. Passivation behavior

Fig. 2(a) presents the cyclic potentiodynamic polarization curves of 316L stainless steel in a 0.5 mol/L H_2SO_4 solution. As the applied potential shifted in the anodic direction, the polarization exhibited a characteristic progression through the active dissolution, passivation onset, sustained passivation, and transpassive regions, as typically observed in austenitic stainless steel within H_2SO_4 environments [46,47]. The polarization curves of the 316L stainless steel exhibit broad passivation that facilitates the formation of a stable and compact passivation films. Based on the stable passivation region in Fig. 2(a), 0.5 V was selected as the passivation potential for subsequent experiments. The voltage of the stable passivation zone serves as a standard for subsequent passivation voltage. When exposed to acidic solution, the passivation films may change as a result of the metal dissolving or oxides and hydroxides forming, ultimately trending towards dynamic equilibrium. Fig. 2(b) presents the current density response curve measured at a passivation potential of 0.5 V, where the passivation films on the surface of 316L stainless steel rapidly nucleate and grow during the initial stages of polarization, causing the current density to quickly decrease with increasing polarization time. As polarization progresses, there is a slight growth of the passivation films, and the current density remains relatively stable, eventually approaching zero, indicating that the prepared passivation films have good quality and stability. Different phases in the current density response curve (double logarithmic curve log$i$ - log$t$) are

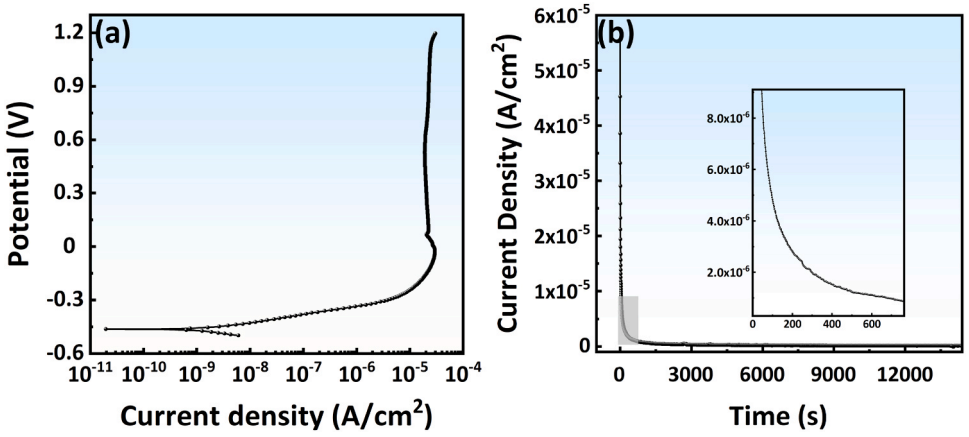

Fig. 2. Electrochemical behavior of 316L stainless steel: (a) Polarization curves; (b) Time evolution of the passivation current density.

divided into three stages [48–50]. In the initial stage, the anodic current density remains largely stable, suggesting that the growth of the passivation films is balanced by their dissolution, resulting in no net film growth. During the second stage, a decline in current density with polarization time marks the transition period. Finally, in the third stage, as the metal undergoes dissolution and the passivation films develop, the current density decreases logarithmically with continued polarization.

3.2. Composition, structure and micromorphology of passivation films

To compare the compositional characteristics of the passivation films on NP and AP samples, XPS was utilized to examine the metallic, oxidized, and hydrolyzed states of Cr 2p, Fe 2p, and O 1s. The spectra for Mo and Ni were excluded from the analysis due to their weak signals and the absence of significant changes. After deconvolution, the Cr spectrum revealed two primary peaks: Cr 2p3/2 and Cr 2p1/2. Notably, Cr 2p3/2 was further resolved into three component peaks: Cr metal (573.16 eV), Cr_2O_3 (575.57 eV), and $Cr(OH)_3$ (577.48 eV). Similarly, Cr 2p1/2 was deconvoluted into three distinct peaks: Cr metal (582.52 eV), Cr_2O_3 (585.43 eV), and $Cr(OH)_3$ (587.58 eV) [51–54], as seen in Fig. 3(a, d). Following sulfuric acid passivation, the Cr_2O_3 content within the passivation films increased, a phenomenon attributable to the formation of the -Cr-O-Cr- bond, which enhanced the films stability and protective efficacy. The dense arrangement of Cr atoms allowed oxygen ions to a bridge, forming continuous clusters of Cr_2O_3, a structure crucial for protecting the substrate. It is these continuously covered Cr_2O_3 clusters that are key to the protective effectiveness of the passivation films, ensuring that it impedes the ingress of hydrogen [55].

The spectra of Fe were deconvoluted to reveal two primary peaks: Fe 2p3/2 and Fe 2p1/2. The Fe 2p3/2 peak was further resolved into four component peaks, namely Fe metal (706 eV), FeO (707.68 eV), Fe_2O_3 (709.79 eV), and FeOOH (712.17 eV). Similarly, the Fe 2p1/2 peak was decomposed into three component peaks: Fe metal (719.05 eV), FeO (721.60 eV), and Fe_2O_3 (722.68 eV), FeOOH (723.66 eV) [56,57], as illustrated in Fig. 3(b, e). Fe^{2+} predominantly exists in the form of FeO, while Fe^{3+} is mainly found in the forms of Fe_2O_3 and FeOOH. After electrochemical passivation, the Fe^{2+}/Fe^{3+} ratio decreased from 0.51 to 0.43, indicating an increase in the formation of Fe^{3+}. It was also found that the passivation films might contain magnetite (Fe_3O_4), and surface Fe_3O_4 can decompose into FeO and Fe_2O_3 [58]. It was calculated

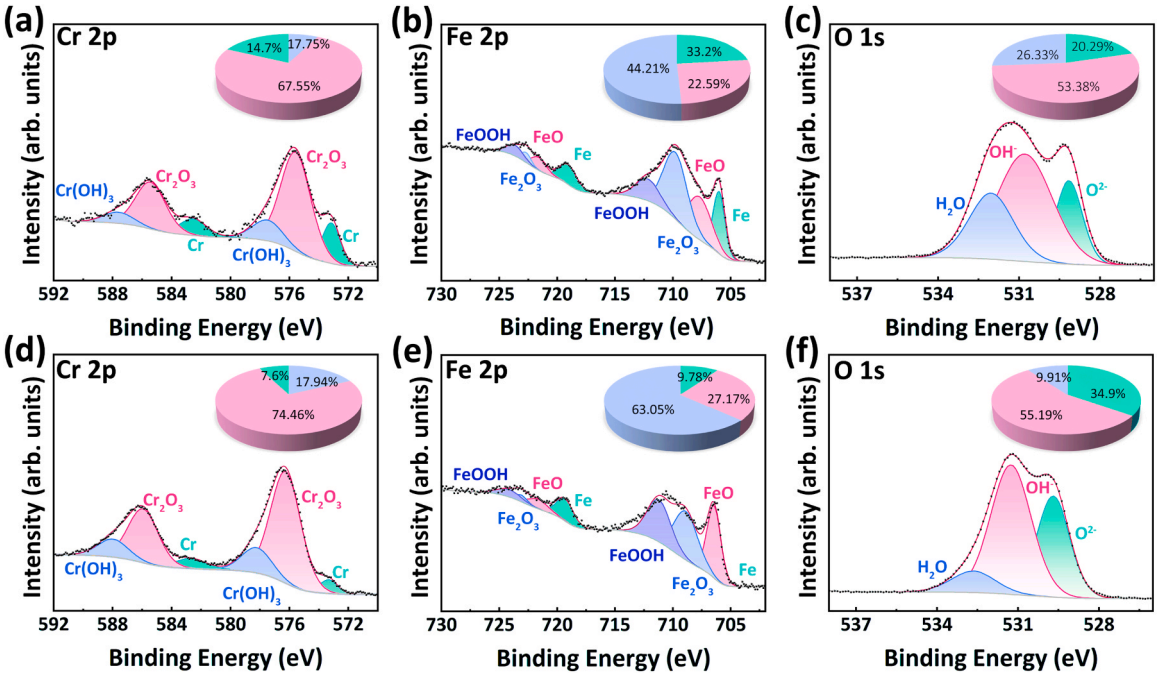

Fig. 3. XPS spectra of the (a, d) Cr 2p; (b, e) Fe 2p; (c, f) O 1s compounds in the (a-c) NP and (d-f) AP samples, along with pie charts showing compound composition.

analytically that the Cr/Fe ratio in AP is 0.78, significantly higher than 0.44 in NP. This result indicates a substantial enrichment of Cr during the AP, leading to the formation of a higher content of Cr_2O_3 on the steel surface. Thus, sulfuric acid passivation not only enhances Cr content within the passivation films but also forms the more protective and denser surface films.

As illustrated in Fig. 3(c, f), the O 1s peak was deconvoluted into three main component peaks: O^{2-} (529.15 eV), OH^- (530.78 eV), and H_2O (532.03 eV), representing metal oxides, metal hydroxides, and water molecules that are adsorbed on the films, respectively [59]. After passivation treatment, the O^{2-}/OH^- ratio increased from 0.38 to 0.63, indicating a greater conversion of hydroxides into oxides, which is consistent with the corresponding changes in the Cr 2p and Fe 2p spectra. Metal oxides were observed to exhibit greater stability compared to metal hydroxides, attributed to their lower number of active sites [60]. The increase in the O^{2-} content suggests that during the electrochemical passivation process, the -M-O-M- structure forms more readily compared to -M-OH-M-. Applying an external voltage accelerates the conversion from OH^- to O^{2-}, diminishing the presence of active sites and thereby enhancing the protective effectiveness of the passivation films. Although the passivation films are primarily composed of oxides, XPS results show that the hydroxide signal exceeds that of oxides. This phenomena can be explained by the continuous potential polarization that forms the passivation films on 316L stainless steel in a sulfuric acid solution. Due to the hydrophilic nature of the metal oxide surface, OH^- in the solution readily adsorb onto the passivation films surface and form surface hydroxyl groups in these areas. These adsorbed hydroxyl groups produce a strong XPS signal [61].

Using ToF-SIMS, a thorough examination of the surface chemical composition of four types of 316L stainless steel samples was performed. The depth profiles of negative ions are displayed in Fig. 4(a, c). It should be emphasized that the selected ions do not represent the actual stoichiometry of the species within the sample but are appropriate markers for the studied species. As ToF-SIMS is a non-quantitative technique, the ion intensities in the depth profiles are influenced by strong matrix effects during ion emission. Consequently, these intensities reflect relative signals rather than absolute concentrations of the associated species in the sample. However, variations within the intensity of a single ion provide insights into the depth-dependent distribution of that species. Secondary ions such as CrO_2^-, $CrOH^-$, FeO_2^-, $FeOH^-$, NiO_2^-, MoO_3^-, $^{18}O^-$, and $^{18}OH^-$ are attributed to the passivation films, while Ni_2^-, Fe_2^- and Cr_2^- are attributed to the metal substrate. The feeble signal of Mo_2^- was disregarded in this analysis. In the analysis of the metal substrate composition, mass numbers representing metal clusters, M_2^-, rather than individual metal anions, M^-, were chosen for calibration. This approach primarily reduces interference from metal ions in metal oxides. Similarly, choosing MO_2^- over MO^- is based on similar considerations. The combination of two oxygen atoms with a metal atom is less likely to arise from the recombination of metal atoms from the metal substrate compared to a combination of one oxygen atom with one metal atom. This selection helps increase the certainty between the corresponding species and the ions generated, thereby ensuring the accuracy and reliability of the analysis results [62]. Besides the oxide and hydroxide films themselves, an alloyed region can be defined, as extensively reported, with nickel enrichment observed between the metal substrate and the oxide layer in austenitic and duplex stainless steels [63,64]. Therefore, the maximum intensity of Ni_2^-, shown by dashed lines in Fig. 4(b, d), determines the location of the alloyed-films interface, and a 3D depth profile analysis of the chosen ions was carried out.

The ion peak intensities of the NP samples mainly appear within the first 17 s of sputtering in Fig. 4(a, b). Comparing the distribution of $^{18}OH^-$ and $^{18}O^-$, $^{18}OH^-$ reaches its peak at 5 s and then rapidly decreases, while $^{18}O^-$ shows a more uniform distribution, peaking at 9 s. This indicates the presence of an inner oxide layer and an outer hydroxide layer, although this structure is not very distinct. For the AP samples, as seen in Fig. 4(c, d), the $FeOH^-$ peak intensity is higher than $CrOH^-$ and appears earlier than other components. Combined with XPS data, this implies that iron hydroxide (FeOOH) makes up the majority of the outer layer. The peaks of CrO_2^- and FeO_2^- appear at 10 and 9 s of sputtering, while the maximum intensities of NiO_2^-, and MoO_3^- are observed at around 5 s. Spectral-related noise typically does not exceed $\pm$ 3, indicating that CrO_2^- and FeO_2^- are more concentrated near the substrate, with the inner layer primarily composed of Cr_2O_3 and Fe_2O_3.

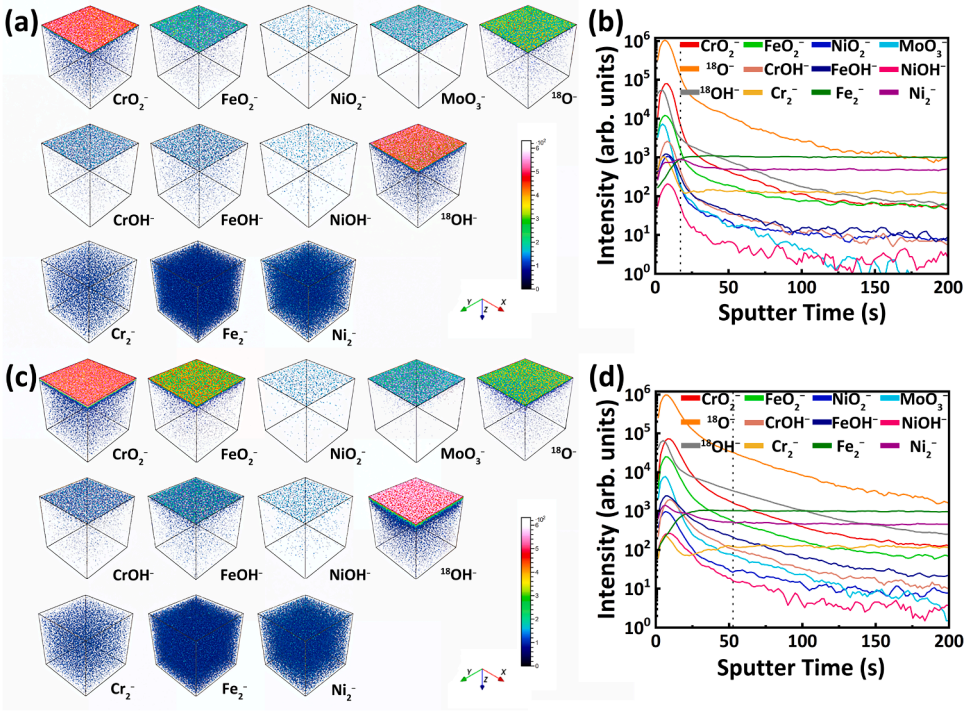

Fig. 4. ToF-SIMS depth profiles of the 316L stainless steel: (a, b) NP; (c, d) AP; (a, c) 3D element distribution map; (b, d) Element depth profile map.

When analyzing $^{18}OH^-$ and $^{18}O^-$, similar behavior is observed. The OH^- peak appears earlier and then quickly decreases, while the $^{18}O^-$ peak appears slightly later and decreases more gradually. This phenomenon confirms that the passivation films formed on 316L stainless steel has a dual-layer structure: an inner oxide barrier layer and an outer exchange layer, consistent with previous reports [19,64,65]. When the Ni intensity peaks at 53 s, it indicates the interface between the passivation films and the metallic substrate. Compared to the NP sample, the increased sputtering time of hydroxides and oxides suggests that the passivation films thickens. The broader and stronger peaks of $FeOH^-$, FeO_2^-, and CrO_2^- indicate the growth and enrichment of Cr and Fe hydroxides and oxides in the passivation films. Due to the assumption that each sample has a nearly constant sputtering yield in depth distribution analysis, accurately determining the thickness of the passivation films from the sputtering depth distribution becomes challenging [21, 66].

For the AP sample, cross-sectional thin sections were cut perpendicular to the alloy surface using focused ion beam and observed using HRTEM. As depicted in Fig. 5(a-b), the cross-sectional layers are displayed sequentially from the top as the protective Pt layer, the passivation films, and the alloy substrate. The thicknesses of the passivation films were measured at 50 different positions, and the average thickness was determined to be approximately 60.04 ± 3 nm, indicating the uniformity of the passivation films. Fast Fourier transform (FFT) analysis of different areas within the passivation films revealed diffraction spots with orthorhombic in Fig. 5(e) and hexagonal in Fig. 5(f) crystal structures, which correspond to FeOOH and Cr_2O_3/Fe_2O_3, respectively, according to previous literature results [67,68]. Inverse fast Fourier transform (IFFT) analysis allowed clear well-ordered atomic arrangements in Fig. 5(g–i). Further analysis using high-angle annular dark field scanning transmission electron microscopy (HAADF-STEM) equipped with energy dispersive X-ray spectroscopy (EDS) showed that the passivation films are rich in O in Fig. 5(j). These findings align with literature results, suggesting that the passivation films in acidic solutions behave as a three-layer model [69–71]. The outermost layer is a hydroxide film, beneath which lies an oxide film, forming over a Ni-rich alloy substrate layer.

316L stainless steel facilitates the early development of Cr-rich oxides at the metal/solution contact by preferentially dissolving its primary component, Fe, and its secondary component, Cr. An outer Fe-rich precipitate layer is then formed by the hydrolysis and redeposition of the dissolved Fe and Cr cations. The passage of metal ions from the substrate and the transfer of oxygen from the solution cause the passivation films to develop and dissolve throughout their growth phase. Over time, a dynamic equilibrium is reached where the growth rate of the film equals its dissolution rate, maintaining a consistent film thickness despite the ongoing movement of the metal/film interface [15]. Additionally, during the growth of the passivation films, crystal growth requires stress accommodation between the film and the substrate, resulting in characteristic morphology at the interface seen in Fig. 5(d). This morphology is likely caused by lattice mismatch and internal stress within the film, forcing the film to adjust its structure to accommodate the substrate [72].

3.3. SSRT tests and fracture morphology

Fig. 6(a) illustrates the engineering stress-strain curves obtained from SSRT testing on four differently treated 316L stainless steel samples at a current density of −20 mA/cm². Corresponding statistical results are presented in Table 3. Additionally, the uniform elongation (δu) and

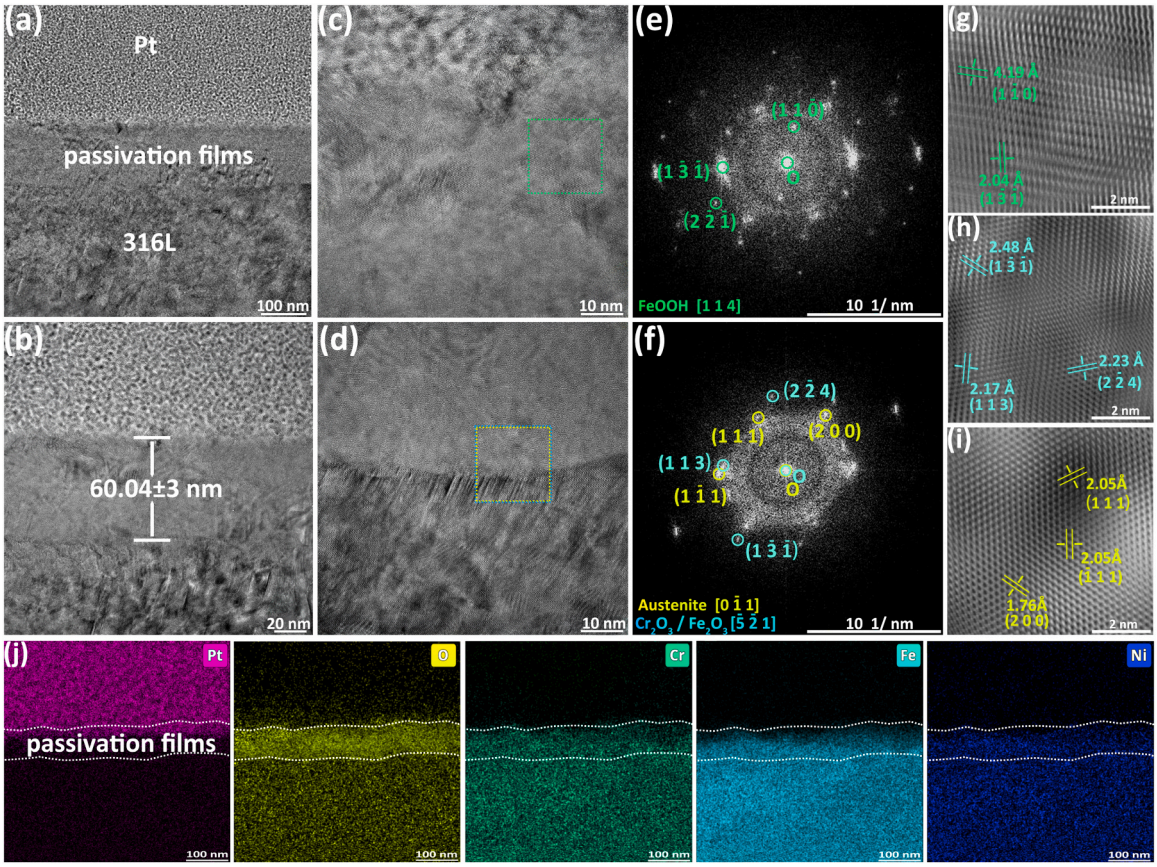

Fig. 5. TEM images of the AP sample: (a) Overall TEM image showing the cross-sectional structure; (b) Magnified view of (a); (c) and (d) Magnified TEM images near the Pt layer and the substrate in the passivation films, respectively; (e) and (f) FFT images corresponding to (c) and (d). (g-h) IFFT images of different spots; (j) EDS image and corresponding elemental maps of Pt, O, Cr, Fe, and Ni.

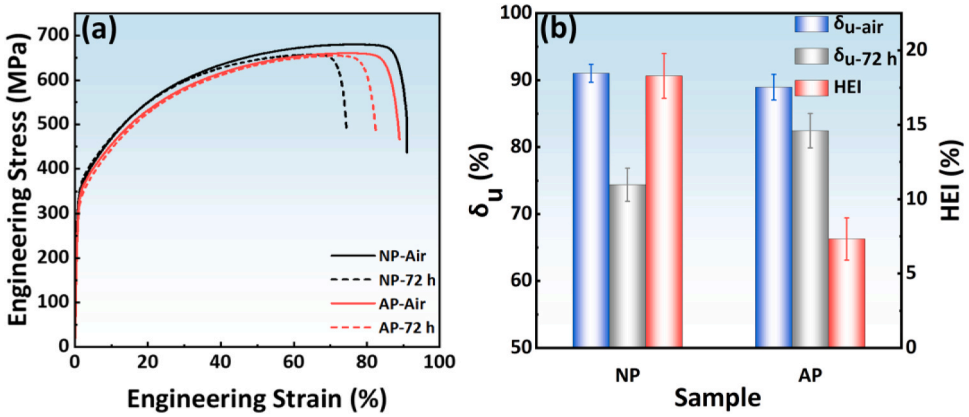

Fig. 6. Mechanical properties from SSRT tests: (a) Engineering stress-strain curves; (b) Summary of δ_u and HEI.

Table 3
SSRT test results and HC of four 316L stainless steel samples.

Sample	σ_y, MPa	σ_{uts}, MPa	δ_u, %	HC, ppm	HEI, %
NP-Air	349 ± 6	680 ± 10	91 ± 1.4	N/A	N/A
NP−72h	346 ± 9	658 ± 7	74.4 ± 2.5	36.71 ± 0.84	18.24 ± 1.51
AP-Air	345 ± 14	660 ± 11	88.9 ± 1.9	N/A	N/A
AP−72h	338 ± 8	654 ± 5	82.4 ± 2.5	25.14 ± 0.72	7.31 ± 1.42

HEI are summarized in Fig. 6(b). According to the statistics, the δ_u for the NP sample was 91 ± 1.4 %, which decreased to 74.4 ± 2.5 % after hydrogen charging. The AP sample showed an δ_u of 88.9 ± 1.9 %, which decreased to 82.4 ± 2.5 % after hydrogen charging. Pre-charged specimens with hydrogen showed less ductility than those without charge. After electrochemical passivation and hydrogen charging, the HEI was reduced by 59.92 %, demonstrating improved resistance to HE. Furthermore, hydrogen content (HC) was 36.71 ± 0.84 ppm in the NP-72h samples, compared to 25.14 ± 0.72 ppm in the AP-72h samples. This further confirms that the passivation films formed by sulfuric acid passivation offers a substantial barrier against hydrogen, effectively slowing hydrogen permeation and thereby enhancing the overall performance of the material.

Fig. 7(a_1–a_3) and (c_1–c_3) depict the fracture surfaces of 316L stainless steel samples NP and AP without hydrogen charging. These images clearly show a uniform distribution of fine dimples formed by micropore aggregation, indicating a ductile dimpled fracture morphology. Conversely, Fig. 7(b_1-b_3) and (d_1-d_3) show the SEM images of the fracture surfaces after NP and AP followed by hydrogen charging for 72 h. A degree of susceptibility of 316L stainless steel to HE was shown by the brittle fracture areas represented by quasi-cleavage planes and secondary fractures along the fracture edges in all hydrogen-charged samples. The red gradient area in the images indicate changes in the depth of the brittle regions affected by hydrogen under both NP and AP conditions. It was observed that the average depth of the brittle region decreased from around 24.74 ± 1.54 μm to 14.53 ± 1.17 μm after electrochemical passivation and hydrogen charging, a reduction of 41.27 %, a change consistent with the reduction in the HEI. Furthermore, this suggests that the passivation films formed by AP provides a certain barrier against hydrogen, effectively mitigating the impact of HE.

3.4. Hydrogen distribution and effects on passivation layers

Using consistent hydrogenation processes and parameters, a detailed analysis of the distribution of specific ions within 316L stainless steel

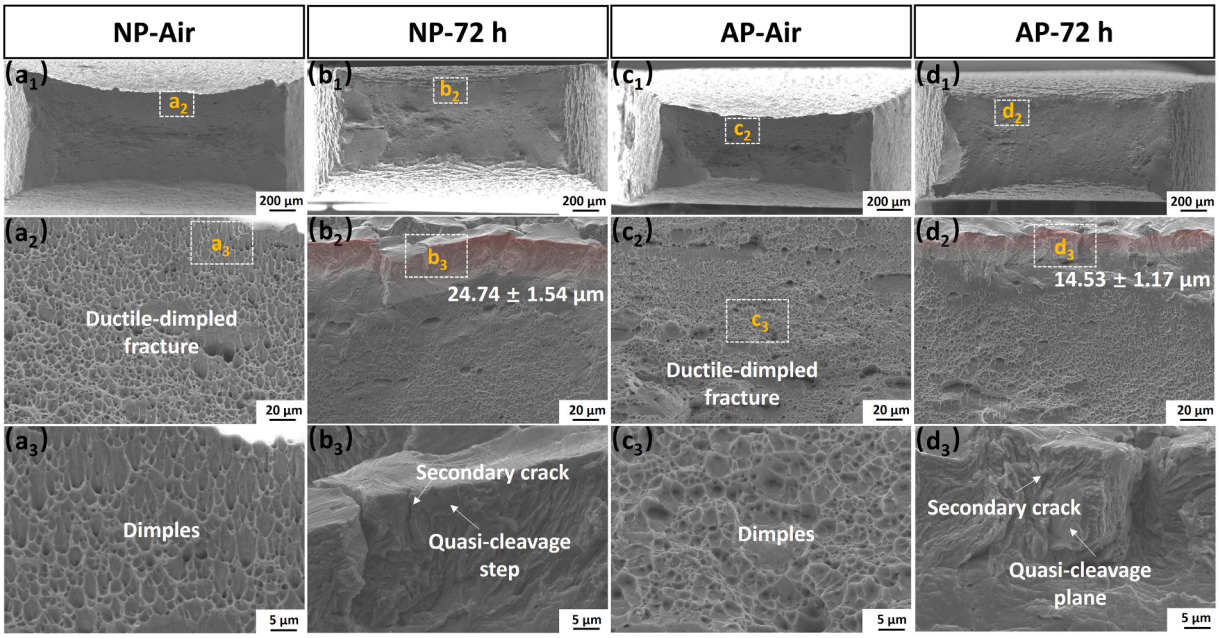

Fig. 7. SEM micrographs of the fracture surfaces: (a_1–a_3) NP-Air; (b_1–b_3) NP-72h; (c_1–c_3) AP-Air; (d_1–d_3) AP-72h.

samples was performed, with data normalized by volume values. For the NP-72h samples, H atoms were found not only concentrated on the surface but also extensively distributed throughout the passivation layer and the metallic substrate in Fig. 8(a-b). Moreover, the hydrogen signal intensity decrease gradually with increasing sputtering time, indicating deeper hydrogen penetration into the substrate. While the inherently slow hydrogen diffusion rate in austenite phase helps to limit hydrogen ingress [73–75], the high surface hydrogen concentration [27] and deeper penetration into the substrate can be attributed to surface adsorption effects and the insufficient density of the naturally formed passivation layer. Moreover, the harsh experimental conditions (e.g., -20 mA/cm^2 cathodic charging for 72 h) exacerbated hydrogen ingress, further damaging the metallic substrate. This effect is evidenced by the uneven coloration in the 3D images of CrO_2^-, FeO_2^- and $FeOH^-$, highlighting the destructive impact of hydrogen on the passivation layer.

In contrast, the AP-72h samples demonstrated a stronger capability to impede hydrogen atoms, with most hydrogen effectively confined to the sample surface and within the passivation layer. The sharp decline in hydrogen signal intensity demonstrates the effectiveness of the electrochemically formed passivation films as a barrier, attributed to their crystalline structure, greater thickness, and enriched oxide composition (Cr_2O_3, Fe_2O_3, and FeOOH), which significantly enhance hydrogen resistance. These properties not only improve the density and stability of the passivation layer but also effectively block hydrogen penetration into the substrate, as indicated by the uniform coloration in the 3D images of CrO_2^- FeO_2^- and $FeOH^-$ in Fig. 8(c-d).

While the inherently slow diffusion rate of hydrogen in the austenite phase contributes to limiting hydrogen penetration, the observed hydrogen distribution highlights that the dominant factor in hydrogen blocking is the quality of the passivation films. The stark differences between the NP and AP samples demonstrate the critical role of electrochemical passivation in mitigating hydrogen ingress, even under severe conditions. These findings illustrate that electrochemical treatment significantly enhances the surface properties of 316L stainless steel and improves the efficacy of passivation films in blocking hydrogen.

3.5. Atomic-scale mechanisms of hydrogen adsorption and diffusion

After determining the structure and hydrogen blocking efficiency of the passivation films, DFT was employed to understand the hydrogen blocking behavior among different materials at the atomic level. The interactions and related energetics between hydrogen and various constituents of the passivation films (FeOOH, Cr_2O_3, Fe_2O_3) were assessed, including the matrix (fcc-Fe). Fig. 9(a–d) displays the representative atomic structures of different materials used in the DFT calculations, along with the diffusion paths of hydrogen atoms in these structures. Initially, the dissolution energy of H at various sites within the structures of FeOOH, Cr_2O_3, Fe_2O_3, fcc-Fe was calculated, as shown in Fig. 9(e). To make comparisons easier, we set the starting point of all structures to 0. The adsorption energy (E_S) of hydrogen is defined as [76]:

$$E_S = E_{(Structure\ with\ H)} - E_{(Structure)} - \frac{E_{(H_2)}}{2} \quad (3)$$

Here, $E_{(structure\ with\ H)}$ represents the total energy of the structure containing an interstitial hydrogen, $E_{(structure)}$ is the total energy of the structure without a hydrogen atom, and $\frac{E_{(H_2)}}{2}$ refers to the energy of a single hydrogen atom in H_2.

Thus, a structure that is more conducive to hydrogen binding has a lower hydrogen adsorption energy, suggesting greater energy release and more stable existence of hydrogen atoms in that structure [77]. Statistical calculations show that the E_s energy at the octahedral sites in fcc-Fe is the lowest at 0.114 eV, consistent with calculated structures [78], verifying the accuracy of the model. For Cr_2O_3 and Fe_2O_3, E_s values are 0.718 eV and 0.888 eV, respectively, while for FeOOH, E_s is the lowest at -3.555 eV, indicating that FeOOH has the greatest hydrogen adsorption capacity. In the passivation films, the outer layer of FeOOH, due to its strong hydrogen adsorption effect, effectively prevents further diffusion of hydrogen into the interior.

Hydrogen diffusion within these materials was further analyzed using the CI-NEB calculations. Fig. 9(f) illustrates the energy variations of hydrogen atoms along their relaxation diffusion paths, where the

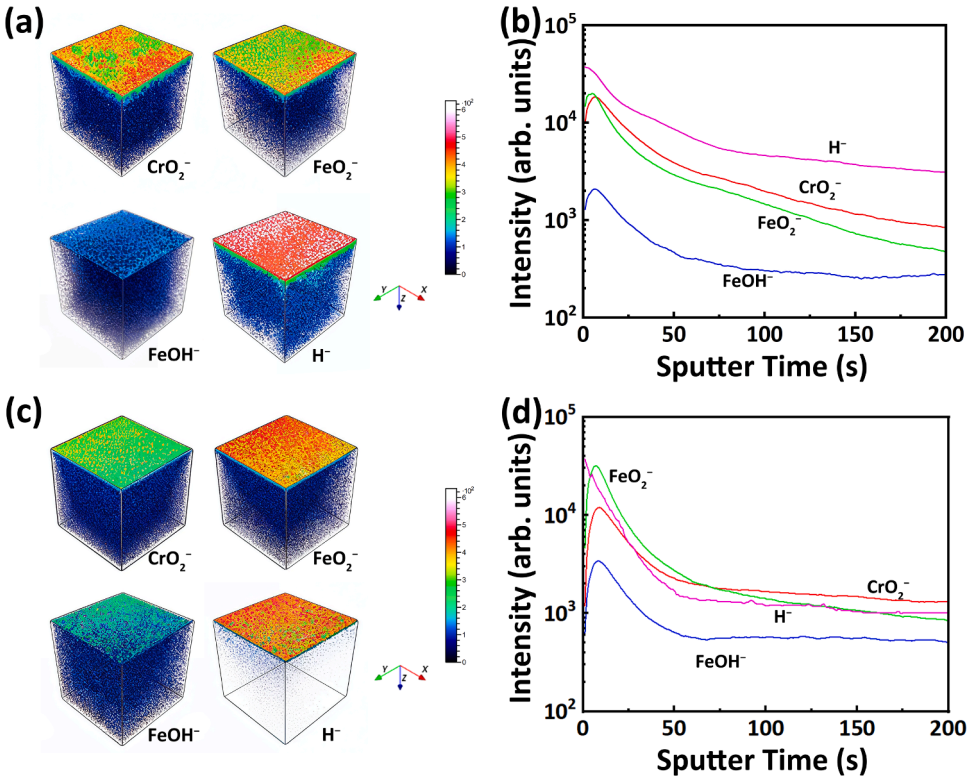

Fig. 8. ToF-SIMS depth profiles for the 316L stainless steel: (a, b) NP-72h; (c, d) AP-72h; (a, c) 3D element distribution map; (b, d) Element depth profile map.

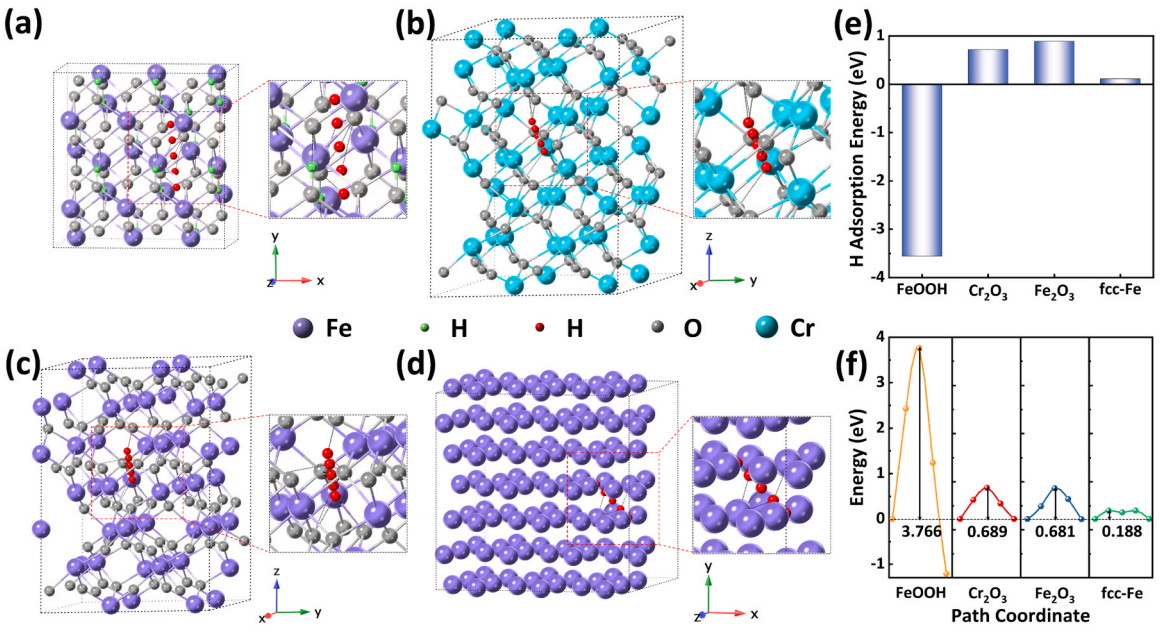

Fig. 9. Hydrogen adsorption and diffusion characteristics: (a–d) Hydrogen diffusion in FeOOH, Cr_2O_3, Fe_2O_3, fcc-Fe structure; (e) Hydrogen adsorption energy; (f) Hydrogen diffusion barriers of FeOOH, Cr_2O_3, Fe_2O_3, fcc-Fe structure.

highest energy barrier corresponds to the transition state location in the migration step. FeOOH exhibits the highest diffusion barrier of 3.766 eV, significantly surpassing those of Cr_2O_3 (0.689 eV) and Fe_2O_3 (0.681 eV). This pronounced barrier underscores the exceptional resistance of FeOOH to hydrogen diffusion, highlighting its highly effective hydrogen impeding action within the passivation films. This resistance substantially slows down hydrogen permeation, thereby greatly enhancing the overall HE-resistant of the passivation films. Furthermore, the tight integration of Cr_2O_3 and Fe_2O_3 with the substrate provides an effective transition layer function, enhancing the structural integrity of the films [79]. This not only stabilizes the growing passivation layer but also augments the overall hydrogen blocking effect of the passivation films through the high hydrogen adsorption capability and diffusion resistance offered by the FeOOH layer. Additionally, the dense, multi-layered configuration of the passivation films significantly limits the connectivity of grain boundaries and defects within the films, thereby reducing potential hydrogen diffusion pathways. In comparison, the diffusion barrier for hydrogen in fcc-Fe is the lowest, at only 0.188 eV, indicating easier diffusion within this structure. However, grain boundaries in the substrate act as preferential pathways for hydrogen diffusion, potentially accelerating hydrogen ingress [80–82].

Hydrogen diffusion coefficients in fcc-Fe were estimated using calculated diffusion barriers and vibrational frequencies in conjunction with the Arrhenius Eq. (2):

$$D\ (T) = 9.157 \times 10^{-8}\ m^2 \Big/ \mathrm{sexp}\left(-\frac{2183.94}{T}\right) \quad (4)$$

The calculated hydrogen diffusion coefficient at room temperature (T = 298 K) is 6.011×10^{-11} m^2/s, as detailed in Table 4, reflecting the relatively easy diffusion of hydrogen within the fcc-Fe structure, consistent with values reported in previous studies [83,84]. The hydrogen diffusion coefficients for the passivation films, Cr_2O_3, Fe_2O_3, and FeOOH, were also calculated. Cr_2O_3 and Fe_2O_3 exhibited diffusion coefficients of 4.609×10^{-19} m^2/s and 5.216×10^{-19} m^2/s, respectively. Most notably, FeOOH demonstrated an exceptionally low diffusion coefficient 5.737×10^{-71} m^2/s, indicating that hydrogen diffusion in this material is nearly negligible. This is attributable to its high diffusion barrier (3.766 eV) and strong hydrogen adsorption capacity (−3.555 eV). It is important to note that these calculations are based on idealized structures of the passivation films. Despite this limitation, the results provide critical insights into the intrinsic hydrogen blocking capabilities of these material.

Table 4
Diffusion coefficients of hydrogen atom in FeOOH, Cr_2O_3, Fe_2O_3 and fcc-Fe.

Composition	l (Å)	ν (HZ)	D (T) (m^2/s)	T (K)	D (T) (m^2/s)
FeOOH	3.3735	2.43	2.765×10^{-7} m^2/s exp(−43,697.43/T)	298	5.737×10^{-71}
Cr_2O_3	3.1945	2.02	2.061×10^{-7} m^2/s exp(−7994.25/T)	298	4.609×10^{-19}
Fe_2O_3	2.9449	1.97	1.708×10^{-7} m^2/s exp(−7901.43/T)	298	5.216×10^{-19}
fcc-Fe	2.4385	1.54	9.157×10^{-8} m^2/s exp(−2183.94/T)	298	6.011×10^{-11}

The calculated energy barriers and diffusion coefficients, consistent with experimental results, highlight the critical role of passivation films in effectively reducing grain boundary diffusion and obstructing overall hydrogen diffusion within the substrate. Additionally, it provides a foundation for refining the design of passivation films and exploring the synergistic effects of multi-layer gradient structures, particularly for applications in hydrogen-rich environments.

4. Conclusions

In this study, passivation films were prepared on the surface of 316L stainless steel using electrochemical methods, and their structure, composition, hydrogen-blocking capabilities, and mechanisms were systematically investigated. The following main conclusions can be drawn:

1. The passivation films formed in a 0.5 mol/L sulfuric acid solution under a 0.5 V treatment for 4 h exhibited a dual-layer structure. The outer layer was primarily composed of orthorhombic FeOOH, while the inner layer consisted of hexagonal Cr_2O_3 and Fe_2O_3. This dual-layer design significantly enhanced the passivation films' hydrogen-blocking performance.

2. Electrochemical passivation treatment significantly reduced the HEI, decreasing from 18.24 % to 7.31 %, a reduction of 59.92 %. The depth of the brittle zone also decreased by 41.27 %, from 24.74 μm to 14.53 μm. SIMS analysis further confirmed that the passivation-treated samples exhibited enhanced hydrogen-blocking capabilities, with hydrogen primarily confined to the surface and passivation layer.
3. DFT calculations indicated that the outer FeOOH layer has a high hydrogen adsorption capacity (−3.555 eV) and significant diffusion barrier (3.766 eV), with an extremely low hydrogen diffusion coefficient (5.737×10^{-71} m^2/s). This further confirms that hydrogen diffusion in this layer is negligible, making it an effective hydrogen barrier. The inner layers of Cr_2O_3 and Fe_2O_3 act as transition layers, strengthening the bonding between the passivation films and the substrate. The synergistic effect of this multilayer structure greatly enhances the hydrogen-blocking performance of the passivation films on the austenitic stainless steel substrate, effectively prolonging the service life of the material in hydrogen-rich environments.
4. This study not only deepens the understanding of the hydrogen-blocking mechanisms of passivation films but also provides a scientific basis for the design of multilayer or gradient films with hydrogen-blocking capabilities, particularly in hydrogen-enriched environments.

CRediT authorship contribution statement

Zhiyu Du: Writing – original draft, Methodology, Investigation, Formal analysis, Conceptualization. **Rongjian Shi:** Writing – review & editing, Supervision. **Zhao Xu:** Software, Data curation. **Zhishan Mi:** Visualization, Formal analysis. **Saiyu Liu:** Methodology. **Yujie Zhu:** Investigation. **Alex A. Volinsky:** Writing – review & editing. **Kewei Gao:** Supervision, Resources. **Xiaolu Pang:** Supervision, Resources, Funding acquisition, Conceptualization.

Declaration of Competing Interest

The authors declare that they have no known competing financial interests or personal relationships that could have appeared to influence the work reported in this paper.

Acknowledgments

The authors acknowledge support from the National Key Research and Development Program of China (No. 2022YFB3709000), National Natural Science Foundation of China (52201060 and 51922002), and the Interdisciplinary Research Project for Young Teachers of USTB (No. FRF-IDRY-22-008).

Data availability

Data will be made available on request.

References

[1] Z.Y. Du, R.J. Shi, X.Y. Peng, K.W. Gao, X.L. Pang, Review on the design of high-strength and hydrogen-embrittlement-resistant steels, Int. J. Miner. Metall. Mater. 31 (2024) 1572–1589, https://doi.org/10.1007/s12613-024-2900-1.
[2] I.M. Robertson, P. Sofronis, A. Nagao, M.L. Martin, S. Wang, D.W. Gross, K. E. Nygren, Hydrogen embrittlement understood, Metall. Mater. Trans. B 46 (2015) 1085–1103, https://doi.org/10.1007/s11663-015-0325-y.
[3] V. Reitenbach, L. Ganzer, D. Albrecht, B. Hagemann, Influence of added hydrogen on underground gas storage: a review of key issues, Environ. Earth Sci. 73 (2015) 6927–6937, https://doi.org/10.1007/s12665-015-4176-2.
[4] S.M. Lee, I.J. Park, J.G. Jung, Y.K. Lee, The effect of Si on hydrogen embrittlement of Fe-18Mn-0.6C-xSi twinning-induced plasticity steels, Acta Mater. 103 (2016) 264–272, https://doi.org/10.1016/j.actamat.2015.10.015.
[5] L.L. Hu, F. Zhong, J. Zhang, S.J. Zhao, Y.Q. Wang, G.X. Cai, T. Cheng, G. Wei, S. F. Jia, D.X. Zhang, R. Yin, Z.Q. Chen, C.Z. Jiang, F. Ren, High hydrogen isotopes permeation resistance in (TiVAlCrZr)O multi-component metal oxide glass coating, Acta Mater. 238 (2022) 118204, https://doi.org/10.1016/j.actamat.2022.118204.
[6] H. Yang, Z.M. Shao, W. Wang, X. Ji, C.J. Li, A composite coating of GO-Al2O3 for tritium permeation barrier, Fusion Eng. Des. 156 (2020) 111689, https://doi.org/10.1016/j.fusengdes.2020.111689.
[7] K.J. Shi, X.Y. Meng, S. Xiao, G.H. Chen, H. Wu, C.L. Zhou, S.H. Jiang, P.K. Chu, MXene coatings: novel hydrogen permeation barriers for pipe steels, Nanomaterials 11 (2021) 2737, https://doi.org/10.3390/nano11102737.
[8] K. Zhang, Y. Hatano, Sealing of pores in sol–gel-derived tritium permeation barrier coating by electrochemical technique, J. Nucl. Mater. 417 (2011) 1229–1232, https://doi.org/10.1016/j.jnucmat.2010.12.276.
[9] X. Xiang, X.L. Wang, G.K. Zhang, T. Tang, X.C. Lai, Preparation technique and alloying effect of aluminide coatings as tritium permeation barriers: a review, Int. J. Hydrogen Energy 40 (2015) 3697–3707, https://doi.org/10.1016/j.ijhydene.2015.01.052.
[10] S. Xiao, X.Y. Meng, K.J. Shi, L.L. Liu, H. Wu, W.Q. Lian, C.L. Zhou, Y.R. Lyu, P. K. Chu, Hydrogen permeation barriers and preparation techniques: a review, J. Vac. Sci. Technol. A 40 (2022) 060803, https://doi.org/10.1116/6.0002178.
[11] V. Maurice, W.P. Yang, P. Marcus, XPS and STM study of passive films formed on Fe-22Cr(110) single-crystal surfaces, J. Electrochem. Soc. 143 (1996) 1182, https://doi.org/10.1149/1.1836616.
[12] V. Maurice, W.P. Yang, P. Marcus, X-Ray photoelectron spectroscopy and scanning tunneling microscopy study of passive films formed on (100) Fe-18Cr-13Ni single-crystal surfaces, J. Electrochem. Soc. 145 (1998) 909–920, https://doi.org/10.1149/1.1838366.
[13] Y. Zhang, Z.N. Wang, S.Y. Huang, H. Liu, Y. Yan, Electrochemical behavior and passivation film characterization of TiZrHfNb multi-principal element alloys in NaCl-containing solution, Corros. Sci. 235 (2024) 112185, https://doi.org/10.1016/j.corsci.2024.112185.
[14] X.Q. Yue, Z.L. Yang, L.Y. Huang, L. Zhang, J. Li, Z.Z. Xue, J.S. Pan, Passivation characteristics of ultra-thin 316L foil in NaCl solutions, J. Mater. Sci. Technol. 127 (2022) 192–205, https://doi.org/10.1016/j.jmst.2022.01.043.
[15] B. Zhang, J. Wang, B. Wu, X.W. Guo, Y.J. Wang, D. Chen, Y.C. Zhang, K. Du, E. E. Oguzie, X.L. Ma, Unmasking chloride attack on the passive film of metals, Nat. Commun. 9 (2018) 2559, https://doi.org/10.1038/s41467-018-04942-x.
[16] R. Kirchheim, B. Heine, H. Fischmeister, S. Hofmann, H. Knote, U. Stolz, The passivity of iron-chromium alloys, Corros. Sci. 29 (1989) 899–917, https://doi.org/10.1016/0010-938X(89)90060-7.
[17] L.J. Oblonsky, M.P. Ryan, H.S. Isaacs, In situ determination of the composition of surface films formed on Fe-Cr alloys, J. Electrochem. Soc. 145 (1998), https://doi.org/10.1149/1.1838577.
[18] P. Keller, H.H. Strehblow, XPS investigations of electrochemically formed passive layers on Fe/Cr-alloys in 0.5 M H2SO4, Corros. Sci. 46 (2004) 1939–1952, https://doi.org/10.1016/j.corsci.2004.01.007.
[19] L.T. Wang, A. Seyeux, P. Marcus, Thermal stability of the passive film formed on 316L stainless steel surface studied by ToF-SIMS, Corros. Sci. 165 (2020) 108395, https://doi.org/10.1016/j.corsci.2019.108395.
[20] Z.C. Wang, A. Seyeux, S. Zanna, V. Maurice, P. Marcus, Chloride-induced alterations of the passive film on 316L stainless steel and blocking effect of pre-passivation, Electrochim. Acta 329 (2020) 135159, https://doi.org/10.1016/j.electacta.2019.135159.
[21] B. Lynch, Z. Wang, L. Ma, E.-M. Paschalidou, F. Wiame, V. Maurice, P. Marcus, Passivation-induced Cr and Mo enrichments of 316L stainless steel surfaces and effects of controlled pre-oxidation, J. Electrochem. Soc. 167 (2020) 141509, https://doi.org/10.1149/1945-7111/abc727.
[22] J. Kruger, I.-N.P. Kruger, Passivity of metals – a materials science perspective, Int. Mater. Rev. 33 (1988) 113–130, https://doi.org/10.1179/imr.1988.33.1.113.
[23] S. Jin, A. Atrens, ESCA-Studies of the structure and composition of the passive film formed on stainless steels by various immersion temperatures in 0.1 M NaCl solution, Appl. Phys. A 45 (1988) 83–91, https://doi.org/10.1007/BF00618768.
[24] Z. Wang, J. Jin, G.H. Zhang, X.H. Fan, L. Zhang, Effect of temperature on the passive film structure and corrosion performance of CoCrFeMoNi high-entropy alloy, Corros. Sci. 208 (2022) 110661, https://doi.org/10.1016/j.corsci.2022.110661.
[25] S. Qian, Y.F. Cheng, Corrosion of X52 steel under thin layers of water condensate in wet gas pipelines, J. Nat. Gas Sci. Eng. 68 (2019) 102921, https://doi.org/10.1016/j.jngse.2019.102921.
[26] M.L. Martin, P. Sofronis, Hydrogen-induced cracking and blistering in steels: a review, J. Nat. Gas Sci. Eng. 101 (2022) 104547, https://doi.org/10.1016/j.jngse.2022.104547.
[27] Y. Yao, L. Qiao, A.A. Volinsky, Hydrogen effects on stainless steel passive film fracture studied by nanoindentation, Corros. Sci. 53 (2011) 2679–2683, https://doi.org/10.1016/j.corsci.2011.05.025.
[28] C. Örnek, F. Zhang, A. Larsson, M. Mansoor, G.S. Harlow, R. Kroll, F. Carlà, H. Hussain, D.L. Engelberg, B. Derin, J. Pan, Understanding passive film degradation and its effect on hydrogen embrittlement of super duplex stainless steel-Synchrotron X-ray and electrochemical measurements combined with CalPhaD and computational studies, Appl. Surf. Sci. 628 (2023), https://doi.org/10.1016/j.apsusc.2023.157364.
[29] X.X. Wei, B. Zhang, B. Wu, Y.J. Wang, X.H. Tian, L.X. Yang, E.E. Oguzie, X.L. Ma, Enhanced corrosion resistance by engineering crystallography on metals, Nat. Commun. 13 (2022), https://doi.org/10.1038/s41467-022-28368-8.
[30] J.G. Yu, J.L. Luo, P.R. Norton, Electrochemical investigation of the effects of hydrogen on the stability of the passive film on iron, Electrochim. Acta 47 (2002) 1527–1536, https://doi.org/10.1016/S0013-4686(01)00882-9.

[31] X.Q. Yue, Z.L. Yang, A. Larsson, H.J. Tang, S. Appelfeller, B. Sefer, A. Preobrajenski, J. Li, L. Zhang, J.S. Pan, Effect of hydrogen on the passivation for ultra-thin 316 L SS foil, NPJ Mater. Degrad. 7 (2023), https://doi.org/10.1038/s41529-023-00398-7.
[32] T.M. Zhang, W.M. Zhao, Y.J. Zhao, K. Ouyang, Q.S. Deng, Y.L. Wang, W. Jiang, Effects of surface oxide films on hydrogen permeation and susceptibility to embrittlement of X80 steel under hydrogen atmosphere, Int. J. Hydrogen Energy 43 (2018) 3353–3365, https://doi.org/10.1016/j.ijhydene.2017.12.170.
[33] M. Qin, Q. Hu, Y.F. Cheng, Passivation of X80 pipeline steel in a carbonate/bicarbonate solution and the effect of oxide film on hydrogen atom permeation into the steel, Int. J. Hydrogen Energy 70 (2024) 1–9, https://doi.org/10.1016/j.ijhydene.2024.05.115.
[34] B. Zhang, X.X. Wei, B. Wu, J. Wang, X.H. Shao, L.X. Yang, S.J. Zheng, Y.T. Zhou, Q. Q. Jin, E.E. Oguzie, X.L. Ma, Chloride attack on the passive film of duplex alloy, Corros. Sci. 154 (2019) 123–128, https://doi.org/10.1016/j.corsci.2019.04.012.
[35] M. Långberg, F. Zhang, E. Grånäs, C. Örnek, J. Cheng, M. Liu, C. Wiemann, A. Gloskovskii, T.F. Keller, C. Schlueter, S. Kulkarni, H. Noei, D. Lindell, U. Kivisäkk, E. Lundgren, A. Stierle, J. Pan, Lateral variation of the native passive film on super duplex stainless steel resolved by synchrotron hard X-ray photoelectron emission microscopy, Corros. Sci. 174 (2020) 108841, https://doi.org/10.1016/j.corsci.2020.108841.
[36] M. Javidi, H.K. Abadeh, H.R. Yazdanpanah, F. Namazi, N.S. Shiri, Synergistic effect of temperature, concentration and solution flow on corrosion and passive film of austenitic SS 304L and 316L in concentrated sulfuric acid, Corros. Sci. 237 (2024) 112306, https://doi.org/10.1016/j.corsci.2024.112306.
[37] H.Y. Du, Q.K. Hu, X.W. Yue, J.W. Jia, Y.H. Wei, L.F. Hou, H. Luo, Q. Wang, H. W. He, H. Wei, X.D. Liu, Effect of Mo on intergranular corrosion behavior in super-austenitic stainless steel, Corros. Sci. 231 (2024) 111986, https://doi.org/10.1016/j.corsci.2024.111986.
[38] X. Wei, B. Zhang, Y. Xu, Z.Y. Chen, X. Li, X. Ma, Transpassivation-induced structural evolution of oxide film on 654SMO super austenitic stainless steel, Corros. Sci. 232 (2024) 112030, https://doi.org/10.1016/j.corsci.2024.112030.
[39] B.P. Gu, H.X. Zhang, Y.S. Wang, G.H. Xu, C.M. Wang, L.Q. Gao, J.H. Chu, Y. C. Yang, Microstructure and corrosion properties of CrMnFeCoNi high entropy alloy coating by temperature field-assisted laser cladding, Surf. Coat. Technol. 494 (2024) 1420–1426, https://doi.org/10.1016/j.surfcoat.2024.131473.
[40] R.J. Shi, Y. Ma, Z.D. Wang, L. Gao, X.S. Yang, L.J. Qiao, X.L. Pang, Atomic-scale investigation of deep hydrogen trapping in NbC/α-Fe semi-coherent interfaces, Acta Mater. 200 (2020) 686–698, https://doi.org/10.1016/j.actamat.2020.09.031.
[41] G. Kresse, J. Hafner, Ab initio molecular dynamics for open-shell transition metals, Phys. Rev. B 48 (1993) 13115–13118, https://doi.org/10.1103/PhysRevB.48.13115.
[42] P.E. Blöchl, Projector augmented-wave method, Phys. Rev. B 50 (1994) 17953–17979, https://doi.org/10.1103/PhysRevB.50.17953.
[43] J.P. Perdew, K. Burke, M. Ernzerhof, Generalized gradient approximation made simple, Phys. Rev. Lett. 77 (1996) 3865–3868, https://doi.org/10.1103/PhysRevLett.77.3865.
[44] S. Arrhenius, Über die Reaktionsgeschwindigkeit bei der Inversion von Rohrzucker durch Säuren, Z. Phys. Chem. 4U (1889) 226–248, https://doi.org/10.1515/zpch-1889-0416.
[45] H.B. Yu, C.F. Chen, R.J. Jiang, P. Qiu, Y.J. Li, Migration of ion vacancy in hydroxylated oxide film formed on Cr: a density functional theory investigation, J. Phys. Chem. C 116 (2012) 25478–25485, https://doi.org/10.1021/jp309898c.
[46] H. Luo, H.Z. Su, G.B. Ying, C.F. Dong, X.G. Li, Effect of cold deformation on the electrochemical behaviour of 304L stainless steel in contaminated sulfuric acid environment, Appl. Surf. Sci. 425 (2017) 628–638, https://doi.org/10.1016/j.apsusc.2017.07.057.
[47] Y. Fu, C.D. Dai, H. Luo, D. Yue, C.W. Du, X.G. Li, The corrosion behavior and film properties of Al-containing high-entropy alloys in acidic solutions, Appl. Surf. Sci. 560 (2021) 149854, https://doi.org/10.1016/j.apsusc.2021.149854.
[48] C. Escrivà-Cerdán, E. Blasco-Tamarit, D.M. García-García, J. García-Antón, R. Akid, J. Walton, Effect of temperature on passive film formation of UNS N08031 Cr-Ni alloy in phosphoric acid contaminated with different aggressive anions, Electrochim. Acta 111 (2013) 552–561, https://doi.org/10.1016/j.electacta.2013.08.040.
[49] H.B. Li, Z.H. Jiang, H. Feng, Q. Wang, W. Zhang, G.W. Fan, G.P. Li, L.Y. Wang, Electrochemical corrosion characteristics of super duplex stainless steel S32750 in LT-MED environment, Int. J. Electrochem. Sci. 10 (2015) 1616–1631, https://doi.org/10.1016/S1452-3981(23)05098-8.
[50] R.M. Fernández-Domene, E. Blasco-Tamarit, D.M. García-García, J. García-Antón, Repassivation of the damage generated by cavitation on UNS N08031 in a LiBr solution by means of electrochemical techniques and Confocal Laser Scanning Microscopy, Corros. Sci. 52 (2010) 3453–3464, https://doi.org/10.1016/j.corsci.2010.06.018.
[51] C.S. Zhou, J. Wang, S.Y. Hu, H.M. Tao, B. Fang, L. Li, J.Y. Zheng, L. Zhang, Enhanced corrosion resistance of additively manufactured 316L stainless steel after heat treatment, J. Electrochem. Soc. 167 (2020) 41504, https://doi.org/10.1149/1945-7111/abc10e.
[52] H. Luo, S.W. Zou, Y.H. Chen, Z.M. Li, C.W. Du, X.G. Li, Influence of carbon on the corrosion behaviour of interstitial equiatomic CoCrFeMnNi high-entropy alloys in a chlorinated concrete solution, Corros. Sci. 163 (2020) 108287, https://doi.org/10.1016/j.corsci.2019.108287.
[53] H. Luo, H.Z. Su, B.S. Li, G.B. Ying, Electrochemical and passive behaviour of tin alloyed ferritic stainless steel in concrete environment, Appl. Surf. Sci. 439 (2018) 232–239, https://doi.org/10.1016/j.apsusc.2017.12.243.
[54] J.W. Ma, H. Luo, X.J. Hu, Z.M. Pan, X.G. Li, Electrochemical study on the effect of hydrogen on the passive film of selective laser melted 316L stainless steel in a proton exchange membrane water electrolyzer environment, Int. J. Hydrogen Energy 48 (2023) 19396–19410, https://doi.org/10.1016/j.ijhydene.2023.02.045.
[55] K. Sieradzki, R.C. Newman, A percolation model for passivation in stainless steels, J. Electrochem. Soc. 133 (1986) 1979, https://doi.org/10.1149/1.2109065.
[56] J.J. Nie, L. Wei, Y. Jiang, Q. Li, H.J. Luo, Corrosion mechanism of additively manufactured 316 L stainless steel in 3.5 wt% NaCl solution, Mater. Today Commun. (2020) 101648, https://doi.org/10.1016/j.mtcomm.2020.101648.
[57] Q. Gao, Y.W. Lu, Q. Yu, Y.T. Wu, C.C. Zhang, R.P. Zhi, High-temperature corrosion behavior of austenitic stainless steel in quaternary nitrate molten salt nanofluids for concentrated solar power, Sol. Energy Mater. Sol. Cells 245 (2022) 111851, https://doi.org/10.1016/j.solmat.2022.111851.
[58] X.Z. Wang, H. Luo, J.L. Luo, Effects of hydrogen and stress on the electrochemical and passivation behaviour of 304 stainless steel in simulated PEMFC environment, Electrochim. Acta 293 (2019) 60–77, https://doi.org/10.1016/j.electacta.2018.10.028.
[59] S. Ningshen, M. Sakairi, K. Suzuki, S. Ukai, The passive film characterization and anodic polarization behavior of 11% Cr ferritic/martensitic and 15% Cr oxide dispersion strengthened steels in different electrolytic solutions, Appl. Surf. Sci. 274 (2013) 345–355, https://doi.org/10.1016/j.apsusc.2013.03.059.
[60] G.O. Okamoto, T. Shibata, Desorption of tritiated bound-water from the passive Film formed on stainless steels, Nature 206 (1965), https://doi.org/10.1038/2061350a0, 1350-1350.
[61] H. Tamura, K. Mita, A. Tanaka, M. Ito, Mechanism of hydroxylation of metal oxide surfaces, J. Colloid Interface Sci. 243 (2001) 202–207, https://doi.org/10.1006/jcis.2001.7864.
[62] B. Lynch, S. Neupane, F. Wiame, A. Seyeux, V. Maurice, P. Marcus, An XPS and ToF-SIMS study of the passive film formed on a model FeCrNiMo stainless steel surface in aqueous media after thermal pre-oxidation at ultra-low oxygen pressure, Appl. Surf. Sci. 554 (2021) 149435, https://doi.org/10.1016/j.apsusc.2021.149435.
[63] H. Ogawa, H. Omata, I. Itoh, H. Okada, Auger electron spectroscopic and electrochemical analysis of the effect of alloying elements on the passivation behavior of stainless steels, Corrosion 34 (2013) 52–60, https://doi.org/10.5006/0010-9312-34.2.52.
[64] Z.C. Wang, E.M. Paschalidou, A. Seyeux, S. Zanna, V. Maurice, P. Marcus, Mechanisms of Cr and Mo enrichments in the passive oxide film on 316L austenitic stainless steel, Front. Mater. 6 (2019) 232, https://doi.org/10.3389/fmats.2019.00232.
[65] Z.C. Wang, F. Di-Franco, A. Seyeux, S. Zanna, V. Maurice, P. Marcus, Passivation-Induced Physicochemical Alterations of the Native Surface Oxide Film on 316L Austenitic Stainless Steel, J. Electrochem. Soc. 166 (2019) C3376, https://doi.org/10.1149/2.0321911jes.
[66] L. Ma, E.M. Pascalidou, F. Wiame, S. Zanna, V. Maurice, P. Marcus, Passivation mechanisms and pre-oxidation effects on model surfaces of FeCrNi austenitic stainless steel, Corros. Sci. 167 (2020) 108483, https://doi.org/10.1016/j.corsci.2020.108483.
[67] N.V. Ter-Oganessian, A.A. Guda, V.P. Sakhnenko, Linear magnetoelectric effect in göthite, α-FeOOH, Sci. Rep. 7 (2017) 16410, https://doi.org/10.1038/s41598-017-16772-w.
[68] Z.S. Mi, L. Chen, H.M. Liu, C.M. Shi, D.C. Wang, X.L. Li, K.F. Gao, L.J. Qiao, Synergistic Effect of Hydrogen and Strain on Electronic Properties of the p-Cr2O3/n-Fe2O3 Interface, J. Phys. Chem. C. 125 (2021) 6351–6358, https://doi.org/10.1021/acs.jpcc.0c11413.
[69] C.-O.A. Olsson, The influence of nitrogen and molybdenum on passive films formed on the austenoferritic stainless steel 2205 studied by AES and XPS, Corros. Sci. 37 (1995) 467–479, https://doi.org/10.1016/0010-938X(94)00148-Y.
[70] J.D. Choundraj, R.G. Kelly, R. Monikandan, P.M. Singh, J. Kacher, Influence of native oxide film on corrosion behavior of additively manufactured stainless steel 316L, Corros. Sci. 217 (2023) 111098, https://doi.org/10.1016/j.corsci.2023.111098.
[71] I. Olefjord, B.-O. Elfstrom, The Composition of the Surface during Passivation of Stainless Steels, Corrosion 38 (1982) 46–52, https://doi.org/10.5006/1.3577318.
[72] G. Abadias, E. Chason, J. Keckes, M. Sebastiani, G.B. Thompson, E. Barthel, G. L. Doll, C.E. Murray, C.H. Stoessel, L. Martinu, Review article: stress in thin films and coatings: current status, challenges, and prospects, J. Vac. Sci. Technol. A 36 (2018) 020801, https://doi.org/10.1116/1.5011790.
[73] A. Turk, S.D. Pu, D. Bombac, P.E.J. Rivera-Díaz-del-Castillo, E.I. Galindo-Nava, Quantification of hydrogen trapping in multiphase steels: Part II - Effect of austenite morphology, Acta Mater. 197 (2020) 253–268, https://doi.org/10.1016/j.actamat.2020.07.039.
[74] L.C.D. Fielding, E.J. Song, D.K. Han, H.K.D.H. Bhadeshia, D.W. Suh, Hydrogen diffusion and the percolation of austenite in nanostructured bainitic steel, P. Roy. Soc. A 470 (2014) 20140108, https://doi.org/10.1098/rspa.2014.0108.
[75] C. Örnek, M. Mansoor, A. Larsson, F. Zhang, G.S. Harlow, R. Kroll, F. Carlà, H. Hussain, B. Derin, U. Kivisäkk, D.L. Engelberg, E. Lundgren, J.S. Pan, The causation of hydrogen embrittlement of duplex stainless steel: phase instability of the austenite phase and ductile-to-brittle transition of the ferrite phase-Synergy between experiments and modelling, Corros. Sci. 217 (2023) 111140, https://doi.org/10.1016/j.corsci.2023.111140.
[76] Z.W. Zhao, C.M. Liu, H.-S. Tsai, J.M. Zhou, Y.Q. Zhang, T.Q. Wang, G.L. Ma, C. H. Qi, M.X. Huo, The strain and transition metal doping effects on monolayer Cr2O3 for hydrogen evolution reaction: the first principle calculations, Int. J. Hydrogen Energy 47 (2022) 37429–37437, https://doi.org/10.1016/j.ijhydene.2021.07.117.

[77] X.R. Fan, Z.S. Mi, L. Yang, H. Su, Application of DFT simulation to the investigation of hydrogen embrittlement mechanism and design of high strength low alloy steel, Materials 16 (2022) 152, https://doi.org/10.3390/ma16010152.
[78] Y.A. Du, L. Ismer, J. Rogal, T. Hickel, J. Neugebauer, R. Drautz, First-principles study on the interaction of H interstitials with grain boundaries in α - and γ -Fe, Phys. Rev. B 84 (2011) 144121, https://doi.org/10.1103/PhysRevB.84.144121.
[79] S.J. Xie, K.Q. Liu, R.Z. Meng, Y.G. Cui, C. Wang, J.Q. Lu, Z.X. Song, D.W. Wang, W. B. Liu, J. Qiu, D. Yun, Formation of intragranular nanocavities in the Cr2O3 layer during the corrosion of Cr3C2+Cr coated Zirlo, Corros. Sci. 233 (2024) 112117, https://doi.org/10.1016/j.corsci.2024.112117.
[80] J. Li, A. Hallil, A. Metsue, A. Oudriss, J. Bouhattate, X. Feaugas, Antagonist effects of grain boundaries between the trapping process and the fast diffusion path in nickel bicrystals, Sci. Rep. 11 (2021), https://doi.org/10.1038/s41598-021-94107-6.
[81] Y. He, Y.J. Su, H.B. Yu, C.F. Chen, First-principles study of hydrogen trapping and diffusion at grain boundaries in γ-Fe, Int. J. Hydrogen Energy 46 (2021) 7589–7600, https://doi.org/10.1016/j.ijhydene.2020.11.238.
[82] A. Oudriss, J. Creus, J. Bouhattate, E. Conforto, C. Berziou, C. Savall, X. Feaugas, Grain size and grain-boundary effects on diffusion and trapping of hydrogen in pure nickel, Acta Mater. 60 (2012) 6814–6828, https://doi.org/10.1016/j.actamat.2012.09.004.
[83] M. Rhode, J. Nietzke, T. Mente, Trapping and diffusion in high-pressure hydrogen charged CoCrFeMnNi high entropy alloy compared to austenitic steel 316L, Int. J. Hydrogen Energy 89 (2024) 772–782, https://doi.org/10.1016/j.ijhydene.2024.09.393.
[84] J.W. Lin, F.D. Chen, F. Liu, D.X. Xu, J. Gao, X.B. Tang, Hydrogen permeation behavior and hydrogen-induced defects in 316L stainless steels manufactured by additive manufacturing, Mater. Chem. Phys. 250 (2020) 123038, https://doi.org/10.1016/j.matchemphys.2020.123038.